

The Effects of Low- and High-Energy Cutoffs on Solar Flare Microwave and Hard X-ray Spectra

Gordon D. Holman

NASA/Goddard Space Flight Center, Greenbelt, MD 20771

`holman@stars.gsfc.nasa.gov`

ABSTRACT

Microwave and hard x-ray spectra provide crucial information about energetic electrons and their environment in solar flares. Both microwave and hard x-ray spectra are sensitive to cutoffs in the electron distribution function. The determination of the high-energy cutoff from these spectra establishes the highest electron energies produced by the acceleration mechanism, while determination of the low-energy cutoff is crucial to establishing the total energy in accelerated electrons. I present computations of the effects of both high- and low-energy cutoffs on microwave and hard x-ray spectra. The optically thick portion of a microwave spectrum is enhanced and smoothed by a low-energy cutoff, while a hard x-ray spectrum is flattened below the cutoff energy. A high-energy cutoff steepens the microwave spectrum and increases the wavelength at which the spectrum peaks, while the hard x-ray spectrum begins to steepen at photon energies an order of magnitude or more below the electron cutoff energy. I discuss how flare microwave and hard x-ray spectra can be analyzed together to determine these electron cutoff energies.

Subject headings: Sun: flares, Sun: radio radiation, Sun: X-rays, gamma rays

1. Introduction

Electrons are accelerated to high, suprathermal energies in solar flares. The total energy contained in these high-energy electrons may be as much as 10% or more of the total flare energy (Hudson & Ryan 1995). Most of these electrons are confined to magnetic loops in the low solar corona until they lose their energy through collisions with the dense plasma of the solar chromosphere and transition region. They are most directly observed through their gyrosynchrotron radiation at microwave frequencies and their bremsstrahlung at x-ray and γ -ray energies. The microwave emission is observed primarily from magnetic loops

in the corona, while the hard x-ray and γ -ray emissions are dominated by thick target bremsstrahlung from electrons in the transition region and chromosphere.

Observations of flares in both microwaves and hard x-rays have shown that the energy distribution of these suprathermal electrons is well described by a power law. The number density of the accelerated electrons can thus be written in the form

$$N(E) = K E^{-\delta} \quad \text{electrons cm}^{-3} \text{ keV}^{-1}, \quad (1)$$

where δ is typically in the range 3–8 (Dennis 1985). When hard x-ray spectra (above any thermal component at the lowest energies) cannot be fitted with a single power law, a double power law will generally provide a good fit.

One of the primary goals of flare research is to determine how suprathermal electrons and ions obtain their energy. One important characteristic of any particle acceleration mechanism is the maximum energy to which particles are accelerated. In principle, the maximum energy to which electrons are accelerated can be determined from high frequency microwave spectra and/or high energy hard x-ray/ γ -ray spectra. In practice, however, spectra have not generally been adequate to establish this energy for individual flares.

The total energy and flux of suprathermal electrons are also important constraints on acceleration mechanisms (Miller et al. 1997). These quantities are sensitive to the low-energy cutoff in the electron distribution, since they are determined by the integration of $N(E)E$ and $N(E)v$ over all electron energies. The hard x-ray spectrum flattens at photon energies below the low-energy cutoff in the electron distribution. This flattening has been difficult to identify, however, either because of insufficient spectral resolution and the high minimum photon energy detectable by the hard x-ray spectrometers (typically 20 keV), or because of the presence of thermal bremsstrahlung at low energies.

The low-energy cutoff may in fact be determined by the spectral transition from thermal to nonthermal bremsstrahlung (Holman & Benka 1992). The suprathermal electrons are likely to be the nonthermal tail of the observed hot thermal plasma. The low-energy cutoff is then the critical break energy between the collisional thermal electrons and the relatively collisionless suprathermal electrons. Benka & Holman (1994) have fit such a hybrid thermal/nonthermal model to high-resolution x-ray spectra from the 1980 June 27 solar flare (Lin et al. 1981). They obtained cutoff energies ranging from 20 keV to 40 keV.

Benka & Holman (1994) also obtained high-energy cutoff energies ranging from 40 keV to 160 keV. In this model an exponential electron distribution is present above the high-energy cutoff.

Gan et al. (2002) have found that many of the broken power-law spectra observed with

BATSE on the Compton Gamma Ray Observatory are consistent with the flattening that results from a low-energy cutoff. They find cutoff energies ranging from 45 keV to 97 keV.

Both microwave and hard x-ray/ γ -ray spectra are becoming better determined with recent progress in instrumentation. The Owens Valley Solar Array (OVSA) can observe solar flares at up to 45 frequencies in the 1–20 GHz range (Gary 1996). The proposed Frequency Agile Solar Radiotelescope (FASR) will obtain higher resolution spectra over an even broader range of radio frequencies (Gary et al. 2001). The Ramaty High Energy Solar Spectroscopic Imager (RHESSI) is obtaining high resolution x-ray/ γ -ray spectra from 3 keV to as high as 17 MeV (Lin et al. 2000). All these instruments are capable of imaging spectroscopy, allowing spatially resolved spectra to be obtained.

In view of the importance of these cutoff energies, the difficulties in establishing them, and the continuing improvements in spectral observations, this paper is devoted to determining the impact of these cutoffs on both microwave and hard x-ray/ γ -ray spectra. The computational methods are described in Section 2 and the impact of low- and high-energy cutoffs on gyrosynchrotron spectra are computed in Section 3. The effects of these cutoffs on thick-target bremsstrahlung spectra are computed in Section 4. Observational difficulties in determining the cutoff energies are discussed in Section 5 and the advantages of analyzing simultaneous microwave and hard x-ray spectra are considered. Conclusions are summarized in Section 6.

2. The Computations

Both the gyrosynchrotron and thick-target bremsstrahlung spectra are computed using numerical codes developed for the interpretation of RHESSI and coordinated radio data. These Fortran 77 codes are available on the Goddard RHESSI Web site at

<http://hesperia.gsfc.nasa.gov/hessi/modelware.htm>.

The gyrosynchrotron code, GYROSPEC, and the thick-target bremsstrahlung code, BREM-THICK, are both explained in accompanying documentation. Their pertinent features are described here.

The gyrosynchrotron code uses the radiation formulae of Ramaty (1969) (and the correction of Trulsen & Fejer 1970) to compute the gyrosynchrotron emission and absorption coefficients in the extraordinary and ordinary modes of polarization. The emission and absorption coefficients are obtained by integrating the gyrosynchrotron emissivity of a single electron times the electron distribution function (or derivatives of the electron distribution

function for the absorption coefficient) over all electron energies. The single electron emissivity consists of a sum of terms for each harmonic of the electron cyclotron frequency. The program determines which cyclotron harmonics contribute to the gyrosynchrotron radiation for a given set of input parameters. Each harmonic term is numerically integrated, starting with the lowest, and summed with the lower contributing harmonics. The inclusion of higher harmonics in the summation continues until the result falls within a specified relative error criterion or the highest contributing harmonic is reached.

For the homogeneous source regions considered here, the intensity of the radiation is related to the emission and absorption coefficients by

$$I_{x,o}(f, \theta) = \frac{j_{x,o}(f, \theta)}{K_{x,o}(f, \theta)} [1 - \exp(-K_{x,o}(f, \theta)L)] \quad \text{erg s}^{-1} \text{ steradian}^{-1} \text{ Hz}^{-1} \text{ cm}^{-2}, \quad (2)$$

where f is the radio frequency, θ is the angle between the direction of propagation of the radiation and the magnetic field, $j_{x,o}$ is the emission coefficient, $K_{x,o}$ is the absorption coefficient, and L is the depth of the source. The subscript x (o) refers to the extraordinary (ordinary) mode of polarization. The radio emission is *optically thick* when $K_{x,o}(f, \theta)L \gg 1$, giving $I_{x,o}(f, \theta) \approx j_{x,o}(f, \theta)/K_{x,o}(f, \theta)$. The emission is *optically thin* when $K_{x,o}(f, \theta)L \ll 1$, giving $I_{x,o}(f, \theta) \approx j_{x,o}(f, \theta)L$.

The observed radio flux is

$$F_{x,o}(f, \theta) = \frac{I_{x,o}(f, \theta)A}{R^2} = \frac{I_{x,o}(f, \theta)A}{2.238 \times 10^7} \quad \text{sfu}, \quad (3)$$

where A is the area of the source in cm^2 , $R = 1 \text{ AU}$, and $1 \text{ sfu} = 10^{-19} \text{ erg cm}^{-2} \text{ s}^{-1} \text{ Hz}^{-1}$.

The thick-target bremsstrahlung code follows the logic of Brown (1971), but uses the relativistic cross section of Haug (1997) and the Elwert (1939) correction to this cross section. The observed x-ray flux is

$$F(E_{ph}) = \frac{nA}{4\pi R^2} \frac{1}{(mc^2)^2} \int_{E_{ph}}^{E_{max}} N(E_o) v_o \left[\int_{E_{ph}}^{E_o} \frac{\sigma(E_{ph}, E) v}{dE/dt} dE \right] dE_o \quad \text{photons cm}^{-2} \text{ s}^{-1} \text{ keV}^{-1}, \quad (4)$$

where $\sigma(E_{ph}, E)$ is the bremsstrahlung cross section, E_{ph} , E , E_{max} , and mc^2 are the photon energy, electron energy, maximum electron energy (high-energy cutoff), and electron rest mass, respectively, in keV, v is the speed of the electron and n is the number density of the target plasma. The collisional energy loss rate provided by Leach & Petrosian (1981) is used: $dE/dt = 4\pi r_o^2 (mc^2) n c^2 \ln \Lambda / v$, where r_o is the classical radius of the electron and $\ln \Lambda$ is the Coulomb logarithm. When $E_{ph} < E_{min}$, the minimum electron energy (low-energy cutoff), the lower limit of the integrals becomes E_{min} . The electron distribution function

and resulting bremsstrahlung are assumed to be isotropic. Note that the thick-target photon flux does not depend on the density of the target plasma.

Although thin-target bremsstrahlung from the corona could provide a more direct comparison with microwave emission, we compute thick-target bremsstrahlung spectra because thick-target bremsstrahlung almost always dominates the flare emission. The effects of the cutoffs studied here on thin-target bremsstrahlung spectra are essentially the same as for thick-target bremsstrahlung.

3. Gyrosynchrotron Spectra

The effects of low- and high-energy cutoffs on microwave spectra are computed for three sets of physical parameters. These are listed in Table 1. The electron density distribution is assumed to be isotropic in pitch angle and to have the form of Equation 1. For a low-energy cutoff of E_{min} and a high-energy cutoff of E_{max} , the total density of suprathermal electrons is

$$N = \frac{K}{\delta - 1} \left(\frac{1}{E_{min}^{\delta-1}} - \frac{1}{E_{max}^{\delta-1}} \right) \text{ cm}^{-3}. \quad (5)$$

For Case 1 when $E_{min} = 10$ keV and $E_{max} = 100$ MeV, for example, $N = 1 \times 10^7 \text{ cm}^{-3}$.

Case 2 differs from Case 1 in that the electron distribution is steeper: the energy index, δ , is 5 instead of 3, putting more of the electrons at low energies. The numerical coefficient K and the depth of the source, L , are increased to enhance the microwave flux and keep the peak flux in the 5 GHz to 10 GHz range (see Section 3.1). Case 3 differs from Case 1 in that the magnetic field strength is lower: B is 100 G instead of 300 G. As a result, higher harmonics of the electron gyrofrequency dominate the microwave radiation. As for Case 2, K and L are increased to enhance the microwave flux and keep the peak flux in the 5 GHz to 10 GHz range.

The angle of emission to the magnetic field, θ , the source area, A , and the thermal plasma density in the source region, n_{th} , are the same for all three sets of input parameters: 45° , $1 \times 10^{18} \text{ cm}^2$, and $6.08 \times 10^9 \text{ cm}^{-3}$, respectively. The plasma density of $6.08 \times 10^9 \text{ cm}^{-3}$ gives an electron plasma frequency of 700 MHz. Gyrosynchrotron radiation is not emitted below the electron plasma frequency. I do not vary these parameters in this paper because doing so does not provide any qualitatively new results. Their impact on microwave spectra has been studied in previous papers (e.g., Ramaty 1969; Benka & Holman 1992).

The spectra are obtained by computing the gyrosynchrotron fluxes at 400 frequencies ranging from 700 MHz to 20 GHz. The degree of circular polarization (fractional polariza-

tion) is given by

$$r_c = \frac{F_o - F_x}{F_o + F_x} \quad (6)$$

The radiation is 100% polarized in the ordinary mode when $r_c = 1$, and 100% polarized in the extraordinary mode when $r_c = -1$. The radio emission is referred to as o-mode when the ordinary mode dominates so that $r_c > 0$, and as x-mode when the extraordinary mode dominates and $r_c < 0$.

3.1. Low-Energy Cutoff

In this subsection I fix the high-energy cutoff at 25.6 MeV ($\gamma = 51$, where $E = (\gamma - 1)mc^2$). This cutoff energy is high enough that it does not significantly affect the radio spectra below 20 GHz.

Figure 1 shows flux and polarization spectra for Case 1 (see Table 1) for a sequence of low-energy cutoffs. In Fig. 1a and subsequent figures the top panel shows the extraordinary mode flux, the center panel shows the ordinary mode flux, and the bottom panel shows the degree of circular polarization. Extraordinary mode radiation is not emitted below the extraordinary mode cutoff frequency, $f_x = \sqrt{f_p^2 + f_B^2/4} + f_B/2$, where f_p is the plasma frequency and f_B is the gyrofrequency, at 1.24 GHz. Therefore, between 700 MHz and 1.24 GHz the radiation is 100% polarized in the ordinary mode.

As the radio frequency drops below the frequency of peak emission (about 7 GHz for the x-mode in Fig. 1a) the spectra become optically thick ($K_{x,o}L \gg 1$, see Eq. 2). As the radio frequency increases above this peak frequency the spectra become optically thin ($K_{x,o}L \ll 1$). The radiation is polarized predominantly in the o-mode at the optically thick frequencies and in the x-mode at the optically thin frequencies.

The structure in the spectra, most evident at the optically thick frequencies, is a consequence of the low harmonics of the gyrofrequency (840 MHz for $B = 300$ G). The higher harmonics are close together and broad, producing a smooth spectrum at higher frequencies. The low harmonics, however, do not overlap and blend as much as the higher ones, producing this structure (see Fig. 3 of Benka & Holman 1992). The harmonics fall in the valleys of the spectral structure, because absorption dominates at the optically thick frequencies. The clear valleys in some of the flux spectra at 1.7 GHz, 2.5 GHz, and 3.4 GHz are located at the second, third, and fourth harmonics of the gyrofrequency. These valleys can be a valuable diagnostic of the magnetic field strength in the emission region.

The low-energy cutoffs for the four spectra shown in Fig. 1a are at 10 keV (solid line),

50 keV (dotted), 100 keV (dashed), and 200 keV (dot-dash), respectively. The effect of the increasing low-energy cutoff is to enhance and flatten the optically thick portion of the spectrum and smooth out the harmonic structure. The degree of o-mode polarization mostly decreases and the crossover frequency from o-mode to x-mode polarization decreases from 4.7 GHz to 3.4 GHz. Although the low-frequency spectrum for the 10-keV low-energy cutoff cannot be represented by a power law, the x-mode spectrum can be estimated to have a mean slope of roughly 3.5, especially in the 4 GHz to 6 GHz range. For the low-energy cutoff of 200 keV, the low-frequency slope has flattened to 2.4.

The optically thin emission (above 7 GHz) is not significantly affected by a cutoff energy of 200 keV or less. The high-frequency spectral index (x-mode) is -1.5, as expected (Dulk 1985).

Fig. 1b shows spectra for low energy cutoffs of 200 keV (solid line), 300 keV (dotted), 500 keV (short dash), 1 MeV (dot-dash), and 3 MeV (long dash). The optically thin emission is now affected by the cutoff energies of 300 keV and above. From 200 keV to 500 keV the optically thick part of the spectrum continues to be enhanced while the peak flux diminishes, the frequency at which the peak is located diminishes somewhat, and the optically thin spectrum begins to flatten. The crossover from o-mode to x-mode polarization drops to 1.5 GHz for the 500 keV cutoff energy. For cutoff energies of 1 MeV and above, all of the emission is optically thin. As the cutoff energy increases the radio flux diminishes at all energies and the spectrum approaches that for emission from relativistic, monoenergetic electrons. Except near and below the x-mode cutoff frequency, the radiation is polarized in the extraordinary mode (i.e., the emission is dominated by x-mode radiation and r_c is negative).

A plot similar to the top panels of Fig. 1 has been presented by White & Kundu (1992, Fig. 1), but with low spectral resolution and $\delta = 4$. They also note the impact of relatively low-energy electrons on the optically thick part of the spectrum, and demonstrate that millimeter wavelength radiation is predominantly emitted by electrons with MeV energies.

Figure 2 shows spectra for Case 2 input parameters and low-energy cutoffs at 10 keV (solid line), 50 keV (dotted line), 100 keV (short dash), 200 keV (dot-dash), and 500 keV (long dash). The harmonic structure in the optically thick part of the spectra is more distinct than for Case 1. The steeper electron distribution ($\delta = 5$) puts more of the electrons at low energies, enhancing the absorption at the low harmonics. As for Case 1, however, the harmonic structure is almost gone in the x-mode when the low-energy cutoff is 50 keV. As the cutoff energy increases, the optically thick part of the spectrum is enhanced, the frequency at which the flux spectrum peaks decreases, and the frequency at which the polarization changes to x-mode also decreases. For the low-energy cutoff of 100 keV, the x-mode low-frequency

spectral index is 2.3.

The high-frequency (optically thin) spectrum for the low-energy cutoff of 10 keV in Fig. 2 has a spectral index of -4.4 below 10 GHz and flattens to -3.5 near 20 GHz. The results of Dulk & Marsh (1982) give a spectral index of -3.3. The discrepancy with Dulk & Marsh probably results from the low harmonics contributing to the emission. The tenth harmonic of the electron gyrofrequency is at 8.4 GHz, while the results of Dulk & Marsh are only accurate for harmonics between 10 and 100.

For Case 2 the high-frequency spectrum starts becoming flattened at a lower cutoff energy than for Case 1. Some flattening is seen for a low-energy cutoff of 100 keV and the spectrum is substantially flattened for a cutoff at 200 keV. For the 500 keV cutoff the radiation is optically thin at all frequencies.

Spectra for Case 3 input parameters are shown in Figure 3. The spectra are much smoother since the radiation is dominated by high harmonics. The electron gyrofrequency for the 100 G magnetic field is 280 MHz and the x-mode cutoff frequency is 854 MHz. Therefore the radiation is 100% polarized in the o-mode between 700 GHz and 854 MHz. Most of the radiation is dominated by harmonics above the tenth.

The spectra shown in Fig. 3 are for low-energy cutoffs at 10 keV (solid line), 100 keV (dotted line), 200 keV (short dash), 500 keV (dot-dash), and 1 MeV (long dash). Except at the lowest frequencies, higher energy cutoffs are required to significantly impact the spectra. Nevertheless, the low-frequency spectrum flattens as the cutoff energy increases from a spectral index of about 3.4 when the cutoff energy is 10 keV to 2.4 when the cutoff energy is 500 keV. The frequency at which the polarization changes from o-mode to x-mode does not decrease significantly until the cutoff energy exceeds 200 keV. The frequency at which the spectrum peaks does not change until the cutoff energy exceeds 500 keV.

The high-frequency, optically thin part of the spectra in Fig. 3 is not affected until the cutoff energy approaches 1 MeV. For cutoff energies below 1 MeV the high-frequency spectral index is -1.1, close to the value expected for highly relativistic electrons, $(1 - \delta)/2 = -1.0$. This is flatter than the spectral index of -1.5 obtained from the results of Dulk & Marsh, even though f/f_B is in the range 10–100. This is probably because harmonics greater than 100 contribute significantly to the radiation below 20 GHz. As the spectra for the 1 MeV cutoff energy indicate, the optically thin radiation is only produced by fully relativistic electrons.

It is interesting that for all three cases the low-frequency spectral index comes close to the value expected for highly relativistic electrons, 2.5, as the cutoff energy increases. The power-law shape is lost, however, as the radiation becomes optically thin for higher cutoff energies.

3.2. High-Energy Cutoff

In this subsection I fix the low-energy cutoff in the electron distribution at 10 keV and explore the effects of a high-energy cutoff on the radio spectra. The initial value of the high-energy cutoff is taken to be 25.6 MeV ($\gamma = 51$), which is high enough to not significantly affect the spectra below 20 GHz.

Figure 4 shows spectra for Case 1 input parameters. Spectra are shown for high-energy cutoffs at 25.6 MeV (solid line), 1 MeV (dotted line), 500 keV (dashed line), and 200 keV (dot-dash line). The spectra for the 25.6 MeV cutoff energy are the same as those in Fig. 1a for the 10 keV low-energy cutoff. The optically thin part of the spectra is significantly steepened for a high-energy cutoff of 1 MeV. The spectra becomes steeper as the cutoff energy decreases. The optically thick part of the spectra, on the other hand, is somewhat flattened from the spectral index of about 3.5 for the 25.6 MeV cutoff energy to about 2.9 for the 200 keV cutoff. The peak flux and the frequency at which it occurs decrease. The frequency at which the polarization changes from o-mode to x-mode also decreases. The x-mode polarization increases and the o-mode polarization decreases as the cutoff energy decreases.

The steepened optically thin spectra are no longer well described by a power law. When the cutoff becomes substantial, however, the high-frequency spectra are well described by a simple exponential of the form

$$F_{x,o}(f) = F_{x,o}^0 e^{-(f-f^0)/\Delta f_{x,o}^e}, \quad (7)$$

where $F_{x,o}^0$ is the radio flux in the x-mode or o-mode at frequency f^0 and $\Delta f_{x,o}^e$ is the frequency interval over which the flux drops by $1/e$. The e -folding interval $\Delta f_{x,o}^e$ is nearly the same for both modes of polarization. For the 200 keV cutoff energy in Fig. 4, for example, the flux spectra above 6 GHz are well fitted with $F_x^0 = 1.7$ SFU, $F_o^0 = 0.17$ SFU, $f^0 = 10$ GHz, $\Delta f_x^e = 1.12$ GHz, and $\Delta f_o^e = 1.14$ GHz. For the 500 keV cutoff energy, the flux spectra are well fitted above 12 GHz with $F_x^0 = 43$ SFU, $F_o^0 = 7.8$ SFU, $f^0 = 10$ GHz, $\Delta f_x^e = 2.60$ GHz, and $\Delta f_o^e = 2.70$ GHz.

Figure 5 shows spectra for Case 2 input parameters with high-energy cutoffs at 25.6 MeV (solid line), 1 MeV (dotted line), 500 keV (dashed line), and 200 keV (dot-dash line). The spectra follow the same trends discussed above for Case 1 (Fig. 4). The impact is not quite as large, however, because of the steeper electron distribution. The optically thick part of the spectra is not significantly affected until the cutoff energy drops to 200 keV. The optically thin flux spectra for the 200 keV cutoff energy are well described above 12 GHz by Equation 7 with $\Delta f_x^e = 1.12$ GHz and $\Delta f_o^e = 1.13$ GHz, about the same values obtained for the Case 1 input parameters. For the 500 keV cutoff energy Eq. 7 is only accurate above 15 GHz, with

$$\Delta f_x^e = 2.48 \text{ GHz and } \Delta f_o^e = 2.58 \text{ GHz.}$$

Spectra for the Case 3 input parameters are shown in Figure 6. The spectra are shown for high-energy cutoffs at 25.6 MeV (solid line), 5 MeV (dotted line), 1 MeV (dashed line), and 500 keV (dot-dash line). Since radiation from higher harmonics and higher energy electrons contribute to the spectra, higher cutoff energies have a greater impact on the spectra. The optically thin part of the spectrum is significantly steepened with a cutoff energy of 5 MeV. Almost the entire spectrum has been affected by the 500 keV cutoff energy. The spectral index for the optically thick part of the spectrum decreases from about 3.4 for the 25.6 MeV cutoff energy to about 2.8 for the 500 keV cutoff. The spectra for the 500 keV cutoff energy are well represented above 5 GHz by Eq. 7 with $\Delta f_x^e = 0.96 \text{ GHz}$ and $\Delta f_o^e = 0.97 \text{ GHz}$. The spectra for the 1 MeV cutoff energy are well represented above 6 GHz by Eq. 7 with $\Delta f_x^e = 2.20 \text{ GHz}$ and $\Delta f_o^e = 2.23 \text{ GHz}$.

4. Bremsstrahlung Spectra

Thick-target bremsstrahlung spectra are computed for Cases 1 and 2 of Table 1. For these computations, only the parameters K , δ , and A are used from Table 1, where A is now the area of the bremsstrahlung emitting region. The mean atomic number of the target plasma is taken to be 1.2. The total number density of suprathermal electrons for each spectrum is given by Equation 5.

The bremsstrahlung spectra were computed at 41 photon energies between 3 keV and 32 MeV, or between 3 keV and the upper cutoff energy when it was less than 32 MeV. Spectra with low-energy cutoffs in the electron distribution are presented and discussed in Section 4.1, and high-energy cutoffs are considered in Section 4.2.

4.1. Low-Energy Cutoff

In this subsection I fix the high-energy cutoff at 3.2 GeV so that the spectra are not significantly steepened below 30 MeV. In each plot a reference spectrum is shown with a low-energy cutoff below 3 keV. All fluxes are in photons $\text{s}^{-1} \text{ cm}^{-2} \text{ keV}^{-1}$.

Figure 7 shows thick-target bremsstrahlung spectra for Case 1 input parameters and low-energy cutoffs in the electron distribution at 1 keV (solid line), 10 keV (upper dotted line), 50 keV (upper short dash), 100 keV (upper dot dash), 200 keV (dash and three dots), 300 keV (long dashes), 500 keV (lower dotted line), 1 MeV (lower short dash), and 3 MeV (lower dot dash). All of the spectra flatten below the cutoff energy.

The spectrum without a cutoff (solid line) is not strictly a power law, but is fitted reasonably well over the entire energy range with a spectral index of -1.85. This is somewhat steeper than the expected value of -1.5 when the non-relativistic Bethe-Heitler cross section is used (Brown 1971).

At low photon energies between 3 keV and the cutoff energy the spectra can be approximated by a power law. For the highest low-energy cutoff, 3 MeV, the spectrum is well represented at photon energies below 30 keV by a power law with a spectral index of -1.1. This spectral index is close to the value expected when the simple Kramer’s bremsstrahlung cross section is used, -1.0. Between 30 keV and 3 MeV the spectrum is not well described by a power law.

For the 100 keV cutoff energy the spectrum is well described between 3 keV and 10 keV by a power law with a spectral index of -1.25. Likewise, for the 50 keV cutoff energy, the spectrum between 3 keV and 10 keV is well represented with a power-law index of -1.3 and, for the 10 keV cutoff, with an index of -1.5 below 8 keV. These results indicate that the spectra typically require two orders of magnitude in photon energy below the cutoff energy to flatten to a spectral index on the order of -1.

Figure 8 shows thick-target bremsstrahlung spectra for Case 2 input parameters. The cutoff energies and line styles are the same as for Fig. 7. As for the Case 1 input parameters, the spectrum without a cutoff (solid line) is not strictly a power law, but is fitted reasonably well with a spectral index of -3.8. As before, this is somewhat steeper than the value of -3.5 obtained with the non-relativistic Bethe-Heitler cross section.

For the 3 MeV low-energy cutoff, the low-energy part of the spectrum between 3 keV and 30 keV can be well fitted with a power law with an index of -1.15. For the 100 keV cutoff energy, the spectrum is well represented between 3 keV and 10 keV by a power-law index of -1.32. As for the Case 1 input parameters, the spectra gradually flatten to a spectra index approaching -1 over two orders of magnitude in photon energy below the cutoff energy.

4.2. High-Energy Cutoff

In this subsection the low-energy cutoff is fixed at 1 keV. The spectra are compared to the same reference spectra as in Fig. 7 and Fig. 8, which have the high-energy cutoff at 3.2 GeV.

Figure 9 shows thick-target bremsstrahlung spectra for Case 1 input parameters and high-energy cutoffs in the electron distribution at 3.2 GeV (solid line), 25.6 MeV (dotted

line), 1 MeV (short dash), 500 keV (dot dash), and 200 keV (long dash). For cutoff energies of 1 MeV and below, the spectra are significantly affected at all the photon energies above 3 keV included in the plot. The photon flux is significantly affected by electrons with energies roughly three orders of magnitude greater than the photon energy for this relatively hard electron distribution ($\delta = 3$). The spectrum drops more rapidly below the original power law as the cutoff energy is approached from below. There is, of course, no radiation above the cutoff energy.

The bremsstrahlung spectra for Case 2 input parameters are shown in Figure 10. The cutoff energies and line styles are the same as for Fig. 9. For this relatively soft electron distribution ($\delta = 5$), the flux is significantly affected by electrons with energies up to roughly one order of magnitude above the photon energy. Therefore, the photon flux is not significantly diminished at energies an order of magnitude or more below the cutoff energy. The flux drops rapidly, however, as the cutoff energy is approached from photon energies within an order of magnitude of the cutoff energy.

5. Observational Issues

The observational goal is to determine the energies of the lowest energy and highest energy suprathermal electrons accelerated in solar flares. We have seen that clear breaks appear in both the gyrosynchrotron and the bremsstrahlung spectra when a low-energy or high-energy cutoff is present in the electron distribution. The observational difficulty is clearly identifying breaks in flare spectra as resulting from these cutoffs in the electron distribution.

Both x-ray and microwave spectra are limited to a range of photon energies or frequencies determined by the instrument. Even for a broadband instrument with high spectral resolution within the band, the frequency range over which a spectrum can be determined is usually limited by the intensity of the flare. Since changes in the spectrum typically occur over an order of magnitude or more in frequency (or photon energy), it can be difficult to distinguish a spectral change resulting from a cutoff in the electron distribution from some other change in the spectrum.

A low-energy cutoff appears in the x-ray spectrum as a flattening of the spectrum below the cutoff energy to a spectral index of about -1. The spectrum gradually flattens over two orders of magnitude in photon energy, however, before this spectral index is reached (Sect. 4.1). Therefore, over a limited range of photon energies, the spectrum is likely to be well fit by a double power-law photon spectrum with a low-energy spectral index between -1

and the high-energy index. The range of photon energies available below the break energy in the spectrum is usually restricted by either the lowest energy channel of the detector or the presence of thermal bremsstrahlung.

The impact of the low-energy cutoff on microwave spectra is to flatten the optically thick part of the spectrum and smooth out any harmonic structure (Sect. 3.1). This signature, however, is difficult to distinguish from inhomogeneity in the source region, which can have the same impact. When harmonic structure is observable, the smoothing of the structure is greater in the x-mode than in the o-mode. Therefore, the polarization spectrum may provide an important discriminator between a low-energy cutoff and source inhomogeneity. This requires further study and will be the topic of a future paper.

When simultaneous x-ray and microwave spectra are available, they can be tested for consistency. If a microwave spectrum is consistent with a low-energy cutoff at 100 keV, for example, the x-ray spectrum should flatten below 100 keV if the spectra are from the same distribution of electrons. Similarly, a hard x-ray spectrum that flattens at low energies should be associated with an optically thick microwave spectrum that is flattened and/or smoothed.

The x-ray spectral fits of Benka & Holman (1994) and Gan et al. (2002) provide values for the low-energy cutoff in the distribution of suprathermal electrons. Unfortunately, these fits are not unique. Other models fit the spectra as well. The high-resolution spectra over a wide range of photon energies from RHESSI will allow some spectral models to be rejected, but multiple models will still provide good fits to the data (e.g., Sui et al. 2002). RHESSI's combination of imaging, spectroscopy, and temporal resolution further helps to sort out the models, but the best bet is to have a different, independent view of the energetic electrons. The most powerful test of the models will be the combination of high-resolution x-ray and microwave spectra and images.

A high-energy cutoff appears in the x-ray/ γ -ray spectrum as a steepening of the spectrum that becomes more rapid as the cutoff energy is approached. No radiation is emitted above the cutoff energy. This steepening occurs over one to several orders of magnitude in photon energy, however (Sect. 4.2). Over a more limited range of photon energies, this steepening can be mistaken for a break to a steeper power-law spectrum or, possibly, the spectrum of a very hot, thermal plasma. This is particularly a problem for weak to moderate intensity flares. For these flares, the flux typically becomes undetectable above the background at a photon energy below 200 keV, leaving little range over which to establish the shape of the spectrum. In a recent study of a C7.5 flare observed by RHESSI on 20 February 2002, Sui et al. (2002) found that the spatially integrated spectrum could be equally well fitted by the thick-target bremsstrahlung from a double power-law electron distribution or a power-law

electron distribution with a high-energy cutoff. A power-law distribution with a low-energy cutoff at 47 keV also provided an acceptable fit to the spectrum if bremsstrahlung from a 40 MK thermal plasma contributed to the emission below 30 keV. The photon spectrum was well observed over the energy range 10 keV to 100 keV.

A high-energy cutoff steepens the optically thin part of the microwave spectrum. The spectral shape becomes exponential rather than power law and the x-mode polarization increases (Sect. 3.2). The frequency at which the microwave flux peaks can also decrease and the optically thick part of the spectrum flatten. This steep, exponential spectrum should be identifiable in a high quality microwave spectrum. A potential problem is that the spectrum might be mistaken for gyrosynchrotron radiation from a thermal plasma. The optically thick part of the spectrum from a thermal plasma should not have a spectral index greater than 2, however, while the spectral index from the suprathermal electrons will be greater than 2 (for a homogeneous source region, at least).

The best circumstance would be to detect the high-energy cutoff in simultaneous x-ray and microwave spectra. If the same electron distribution is responsible for both emissions, the effects of the high-energy cutoff should be visible in both spectra. It would be equally interesting if the case for a cutoff were strong in one of the spectra, but the cutoff did not appear in the other spectrum. Much could be learned about electron propagation or acceleration through an effort to understand why the electron distributions are different.

Benka & Holman (1994) found that a spectrum with an exponential high-energy cutoff provided a good fit to the high-resolution spectra of Lin et al. (1981) from the 27 June 1980 flare. More recently, Sui et al. (2002) found that a power-law electron distribution with a high-energy cutoff at 224 keV provides a good fit to the spatially integrated spectrum of the 20 February 2002 flare observed by RHESSI. Unfortunately, simultaneous microwave spectra were not available for either of these flares. Given the sensitivity of the optically thin microwave emission to such a cutoff, simultaneous microwave spectra would provide an important test of these model fits to the x-ray spectra.

Studies of γ -ray spectra from large flares have found that the spectra are typically flatter than the hard x-ray spectra, with the spectral break occurring at a photon energy between 200 keV and 1 MeV (Vestrand 1988; Rieger, Gan & Marschhäuser 1998). Since optically thin microwave emission is often dominated by radiation from the higher energy electrons that contribute to this γ -ray emission, when this spectral flattening is present the high-frequency microwave spectrum will be flatter than expected from the spectral index of the hard x-ray emission. In some cases this may be observed as a spectral break in the optically thin microwave spectrum to a flatter spectrum at high frequencies (Hildebrandt et al. 1998). Evidence that this spectral flattening at γ -ray energies and, therefore, in the

electron distribution at high electron energies, is a property of most flares is provided by a study of simultaneous BATSE hard x-ray spectra and OVSA microwave spectra (Silva, Wang & Gary 2000). These authors studied the x-ray and optically thin microwave spectra of 57 bursts from 27 flares. They found that in 75% of the bursts the microwave spectrum is flatter than that predicted by the hard x-ray spectral index.

The result of Silva et al. indicates that less than 25% of flare spectra will show the steepening from a high-energy cutoff at microwave frequencies or hard x-ray energies. When a high-energy cutoff is present, the microwave spectrum will usually be steepened more than the hard x-ray spectrum. When the magnetic field strength is high, however, the x-ray spectrum can show more steepening than the microwave spectrum. Spectra with high-energy cutoffs from regions where the magnetic field strength exceeds 500 G could be responsible for some of the “flatter microwave spectra” found by Silva et al.

Silva et al. deduced the electron density power-law index from the x-ray spectral index using the relationship $\delta_x = \alpha_x + 1.5$. I find, however, that $\delta_x = \alpha_x + 1.2$ provides a better approximation to the computed bremsstrahlung spectra. I have also found that, for a low magnetic field strength, the relationship between the electron power-law index and the optically thin microwave spectral index can be closer to the result for highly relativistic electrons, $\delta_r = 2\alpha_r + 1$, than the result of Dulk & Marsh, $\delta_r = 1.11\alpha_r + 1.36$. On the other hand, the optically thin spectrum can be steeper than the Dulk & Marsh value before it flattens at higher frequencies (Fig. 2).

The results of Silva et al. are an important step in understanding the relationship between flare x-ray and microwave spectra. A better knowledge of the spectral shapes, and a more detailed modeling of the spectra, are needed before the results can be fully understood, however.

The extent to which the range of electron energies contributing to an observed x-ray spectrum overlaps with the range of electron energies contributing to an observed radio spectrum strongly depends on the magnetic field strength in the radio source. The x-ray bremsstrahlung flux at a given photon energy is determined by electrons with energies ranging from the photon energy to one or several orders of magnitude greater than the photon energy, depending on the energy index δ of the electron distribution. For the 100 G source considered here (Case 3, Figs. 3 & 6), the optically thin radio emission below 20 GHz (and above approximately 10 GHz) is emitted primarily by electrons in the 1–10 MeV energy range. For a flare with weak hard x-ray emission above 100 keV, there is essentially no overlap in the electron energies producing the hard x-ray spectrum below 100 keV and those producing the optically thin radio spectrum. On the other hand, the optically thick radio emission for this case is primarily sensitive to electrons with energies in the range 100 keV – 1 MeV.

Therefore, for the optically thick radio emission the electron energies do overlap with those contributing to the x-ray emission below 100 keV.

For the 300 G sources the radio spectrum is emitted by lower energy electrons. The optically thin part of the spectrum is predominantly emitted by 100 keV – 1 MeV electrons for Case 2, and by 300 keV – 3 MeV electrons for Case 1. The optically thick part of the spectrum is affected by electrons with energies on the order of 10 keV up to energies of about 100 keV for Case 2, or up to about 500 keV for Case 1. Hence there is strong overlap with the electron energies responsible for the hard x-ray emission below 100 keV.

6. Conclusions

As convenient as it is to model x-ray and microwave spectral data with simple single or double power laws in photon energy, more can be learned by fitting these data with spectra computed from simple electron distributions. A double power-law fit to a photon spectrum provides one or two photon spectral indices, a break energy, and the normalization for the photon spectrum. Fitting the emission with a power-law electron density distribution with a high- and/or low-energy cutoff, on the other hand, provides the power-law index of the electron distribution, the minimum and/or the maximum energy of the electrons in the distribution, and information about the density of the nonthermal electrons. The fit gives the electron density per unit energy times the source area or volume and, if the low-energy cutoff is determined, the total suprathermal electron density times the source area or volume. These more physical results are crucial for the comparison of x-ray/ γ -ray data with microwave data, and for the evaluation of electron acceleration and propagation models.

The computing power needed to routinely fit x-ray and microwave spectra with computed bremsstrahlung and gyrosynchrotron spectra has only recently become widely available. This more physical approach to fitting spectra should now be the norm. Although spectra from more detailed models for electron acceleration and propagation can and should be applied to the data, “everyday” spectral fits that are not strongly model dependent need to address the physical properties of the radiating electrons and their environment. The computed spectra that I have explored in this paper are practical for this purpose.

Flare researchers have long appreciated the potential of combining x-ray, γ -ray, and microwave observations for understanding high-energy phenomena in flares. Only recently, however, has the combination of simultaneous high-resolution x-ray/ γ -ray and microwave spectra and images become realizable. In practice, however, these combined datasets are still difficult to obtain. RHESSI is now obtaining a wealth of high-resolution observations

of flares. The Owens Valley Solar Array obtains high-resolution microwave spectra and images of flares, but the imaging capabilities of OVSA are limited and the data are difficult to analyze and interpret. Combined datasets that provide high quality results from both instruments are rare. Nevertheless, the value is great when these simultaneous datasets are obtained. Hopefully the time is not long before these combined datasets become routine.

This work was supported in part by the NASA Sun-Earth Connection program. I thank the referee for helping to improve some of the discussion in this paper.

REFERENCES

- Benka, S. G. & Holman, G. D. 1992, *ApJ*, 391, 854
- Benka, S. G. & Holman, G. D. 1994, *ApJ*, 435, 469
- Brown, J. C. 1971, *Sol. Phys.*, 18, 489
- Dennis, B. R. 1985, *Sol. Phys.*, 100, 465
- Dulk, G. A. 1985, *ARA&A*, 23, 169
- Dulk, G. A., & Marsh, K. A. 1982, *ApJ*, 259, 350
- Elwert, G. 1939, *Ann. Physik*, 34, 178
- Gan, W. Q., Li, Y. P., Chang, J., & McTiernan, J. M. 2002, *Sol. Phys.*, 207, 137
- Gary, D. E. 1996, in *ASP Conf. Ser. 93, Radio Emission from the Stars and the Sun*, ed. A. R. Taylor & J. M. Paredes (San Francisco: ASP), 409
- Gary, D. E., Bastian, T. S., White, S. M., & Hurford, G. J. 2001, in *2001 Asia-Pacific Radio Science Conference AP-RASC '01 Proceedings* (Tokyo: Chuo University), 236
- Haug, E. 1997, *A&A*, 326, 417
- Hildebrandt, J., Krüger, A., Chertok, I. M., Fomichev, V. V. & Gorgutsa, R. V. 1998, *Sol. Phys.*, 181, 337
- Holman, G. D. & Benka, S. G. 1992, *ApJ*, 400, L79
- Hudson, H. & Ryan, J. 1995, *ARA&A*, 33, 239

- Leach, J. & Petrosian, V. 1981, ApJ, 251, 781
- Lin, R. P., Schwartz, R. A., Pelling, R. M. & Hurley, K. C. 1981, ApJ, 251, L109
- Lin, R. P., & the HESSI Team. 2000, in ASP Conf. Ser. 206, High Energy Solar Physics – Anticipating HESSI, ed. Ramaty, R., & Mandzhavidze, N. (San Francisco: ASP), 1
- Miller, J. A., Emslie, G. A., Holman, G. D., Cargill, P. J., Dennis, B. R., LaRosa, T. N., Winglee, R. M., Benka, S. G. & Tsuneta, S. 1997, J. Geophys. Res., 102, 14631
- Ramaty, R. 1969, ApJ, 158, 753
- Rieger, E., Gan, W. Q. & Marschhäuser, H. 1998, Sol. Phys., 183, 123
- Silva, A. V. R., Wang, H. & Gary, D. E. 2000, ApJ, 545, 1116
- Sui, L., Holman, G. D., Dennis, B. R., Krucker, S., Schwartz, R. A. & Tolbert, K. 2002, Sol. Phys., in press
- Trulsen, J. & Fejer, J. A. 1970, J. Plasma Physics, 4, 825
- Vestrand, W. T. 1988, Sol. Phys., 118, 95
- White, S. M. & Kundu, M. R. 1992, Sol. Phys., 141, 347

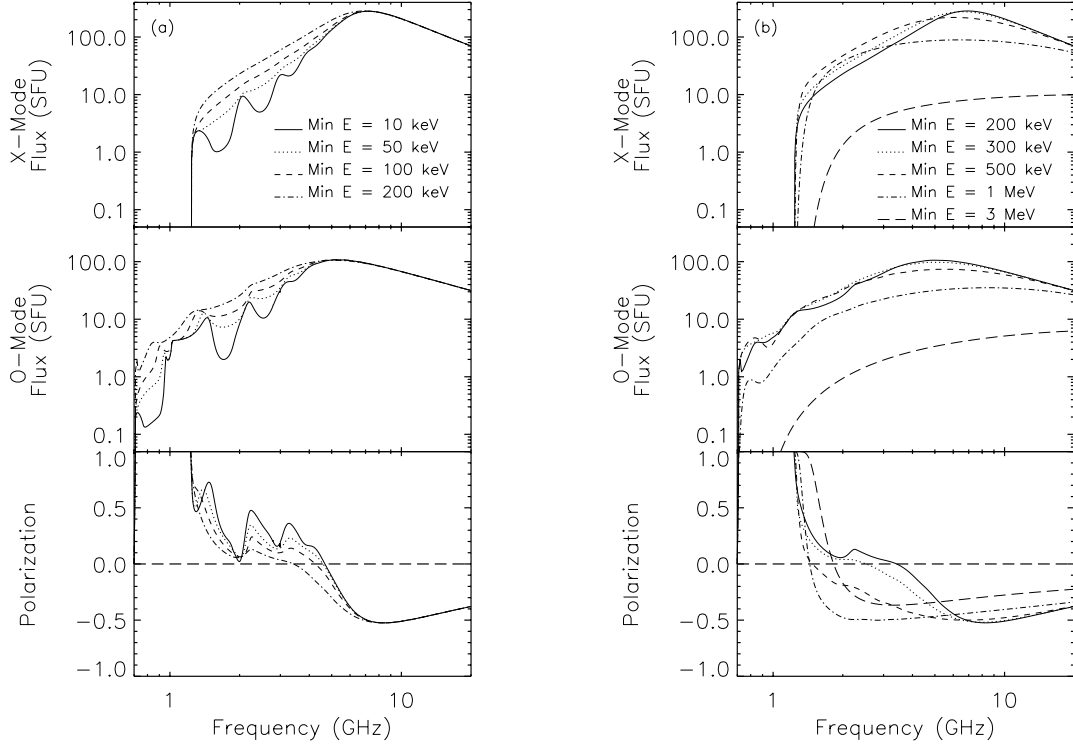


Fig. 1.— Extraordinary-mode flux (top panel), ordinary-mode flux (center panel), and fractional polarization (bottom panel) spectra are plotted over the frequency range 700 MHz to 20 GHz for Case 1 input parameters (see Table 1). The radio fluxes are in solar flux units ($1 \text{ SFU} = 10^{-19} \text{ erg cm}^{-2} \text{ s}^{-1} \text{ Hz}^{-1}$). Positive polarization corresponds to the ordinary mode. (a) Spectra are shown for low-energy cutoffs in the electron distribution at 10 keV (solid line), 50 keV (dotted line), 100 keV (dashed line), and 200 keV (dot-dash line). The high-energy cutoff is fixed at 25.6 MeV. (b) Spectra are shown for low-energy cutoffs at 200 keV (solid), 300 keV (dotted), 500 keV (short dash), 1 MeV (dot-dash), and 3 MeV (long dash).

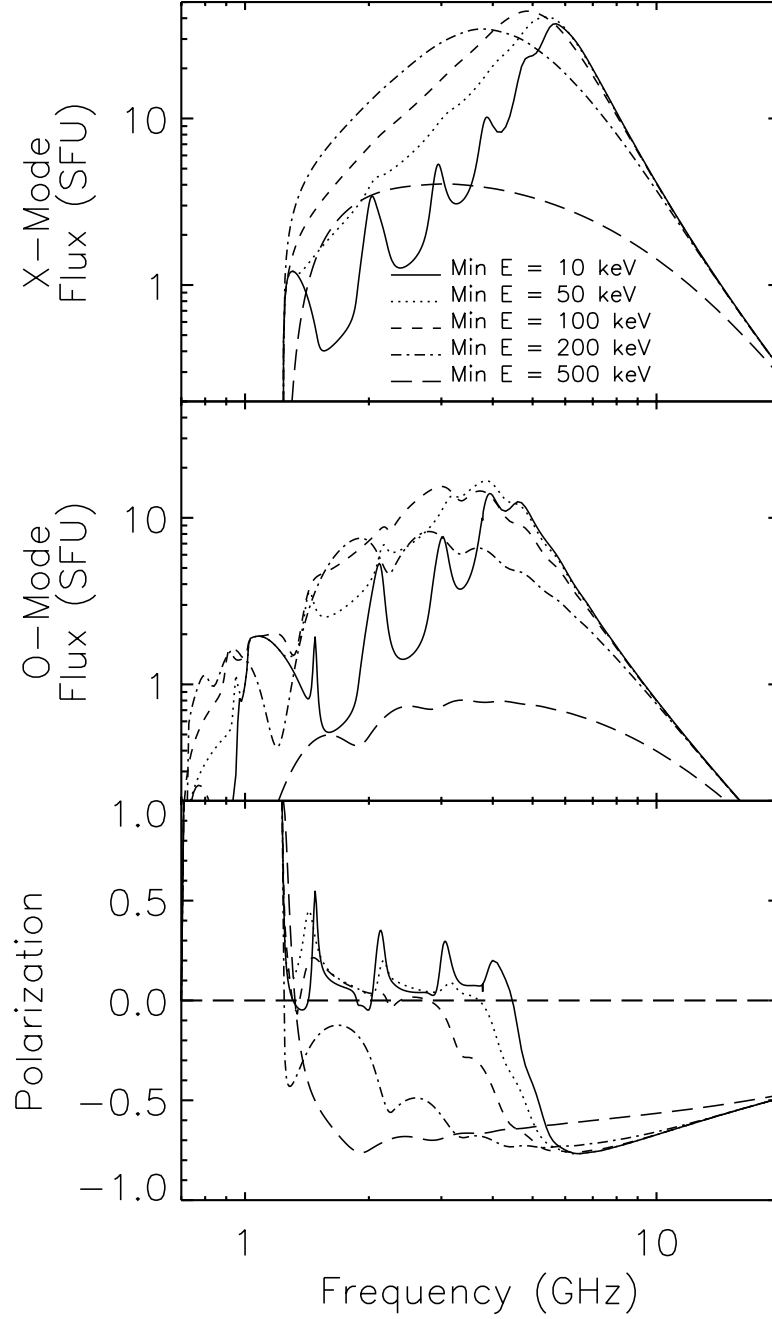


Fig. 2.— Same format as Fig. 1a, but for Case 2 input parameters. Spectra are shown for low-energy cutoffs in the electron distribution at 10 keV (solid line), 50 keV (dotted line), 100 keV (short dash), 200 keV (dot-dash), and 500 keV (long dash). The high-energy cutoff is fixed at 25.6 MeV.

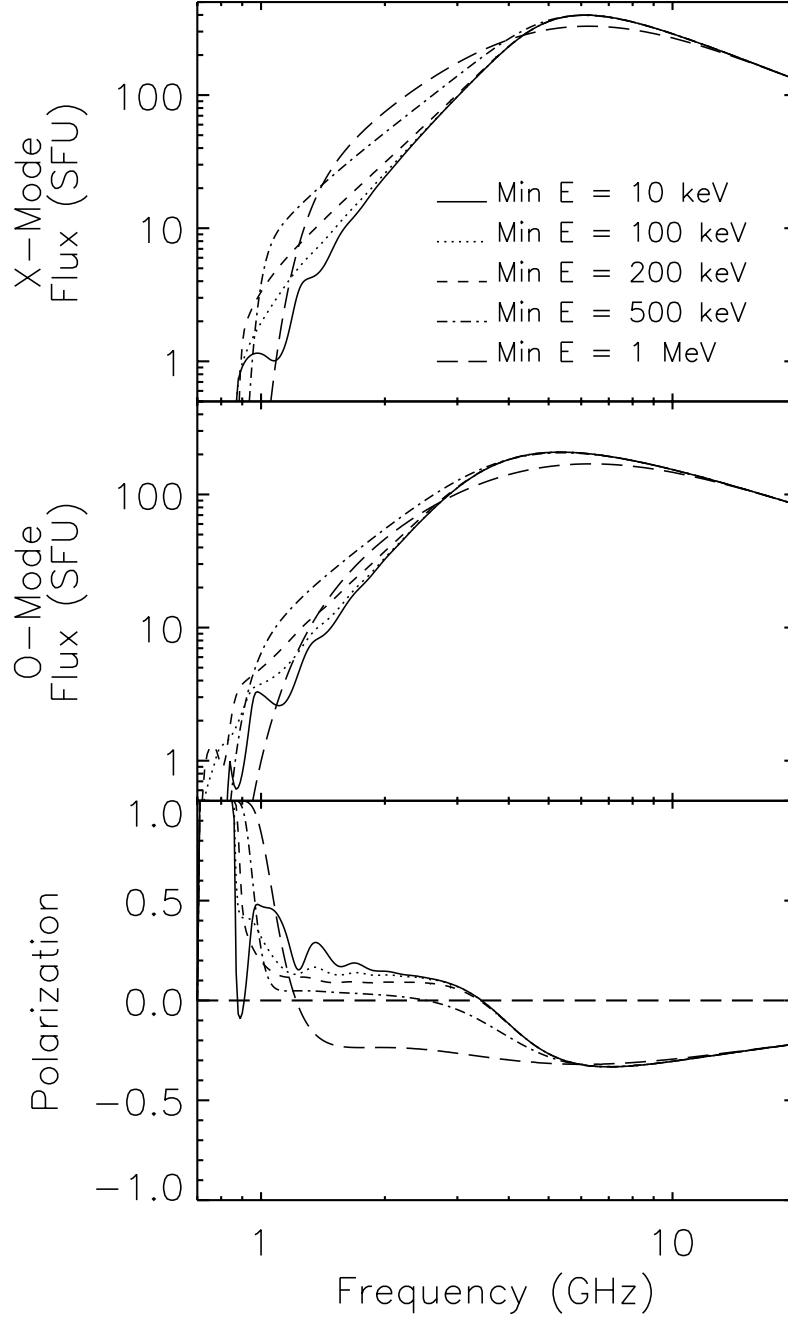


Fig. 3.— Same format as Fig. 1a, but for Case 3 input parameters. Spectra are shown for low-energy cutoffs in the electron distribution at 10 keV (solid line), 100 keV (dotted line), 200 keV (short dash), 500 keV (dot-dash), and 1 MeV (long dash). The high-energy cutoff is fixed at 25.6 MeV.

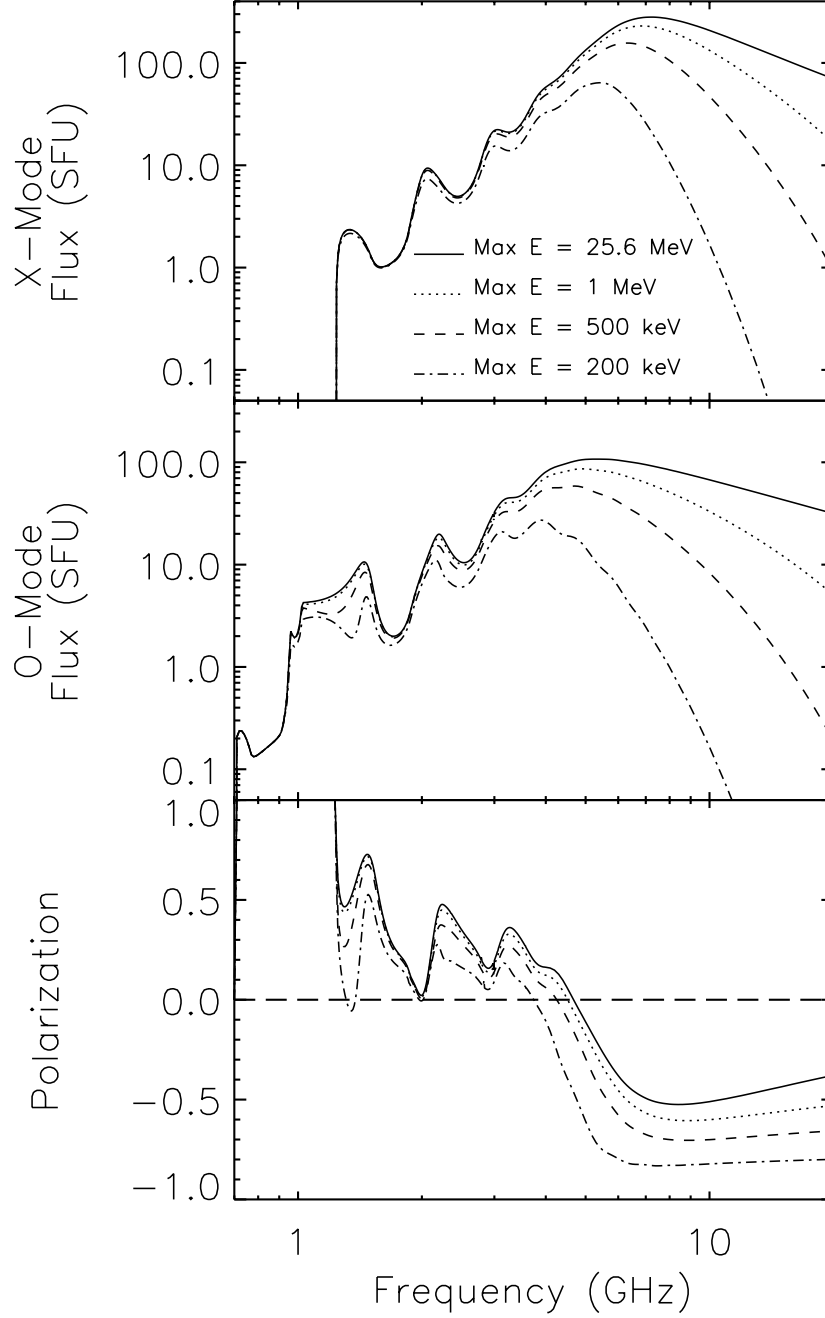


Fig. 4.— Same format as Fig. 1a, but for Case 1 input parameters and high-energy cutoffs in the electron distribution at 25.6 MeV (solid line), 1 MeV (dotted line), 500 keV (dashed line), and 200 keV (dot-dash line). The low-energy cutoff is fixed at 10 keV.

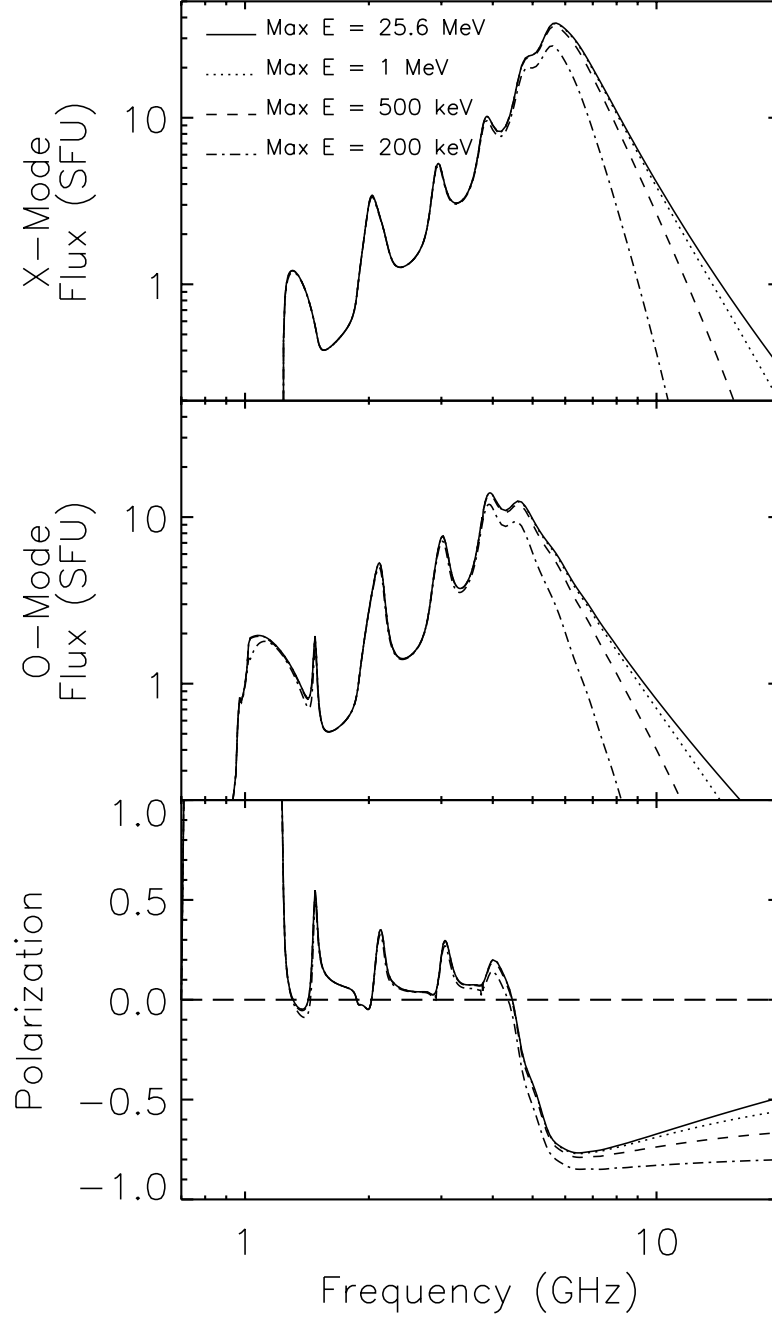


Fig. 5.— Same format as Fig. 1a, but for Case 2 input parameters and high-energy cutoffs in the electron distribution at 25.6 MeV (solid line), 1 MeV (dotted line), 500 keV (dashed line), and 200 keV (dot-dash line). The low-energy cutoff is fixed at 10 keV.

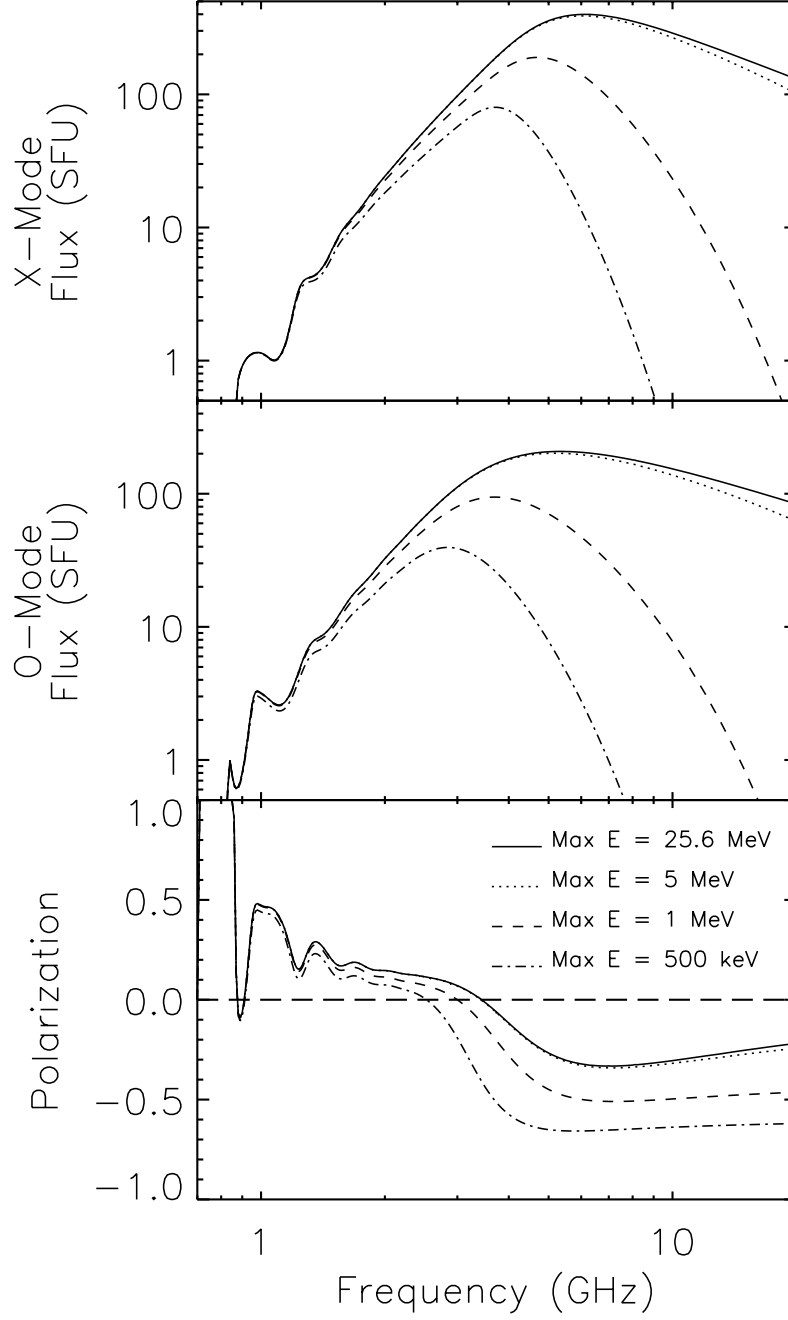


Fig. 6.— Same format as Fig. 1a, but for Case 3 input parameters and high-energy cutoffs in the electron distribution at 25.6 MeV (solid line), 5 MeV (dotted line), 1 MeV (dashed line), and 500 keV (dot-dash line). The low-energy cutoff is fixed at 10 keV.

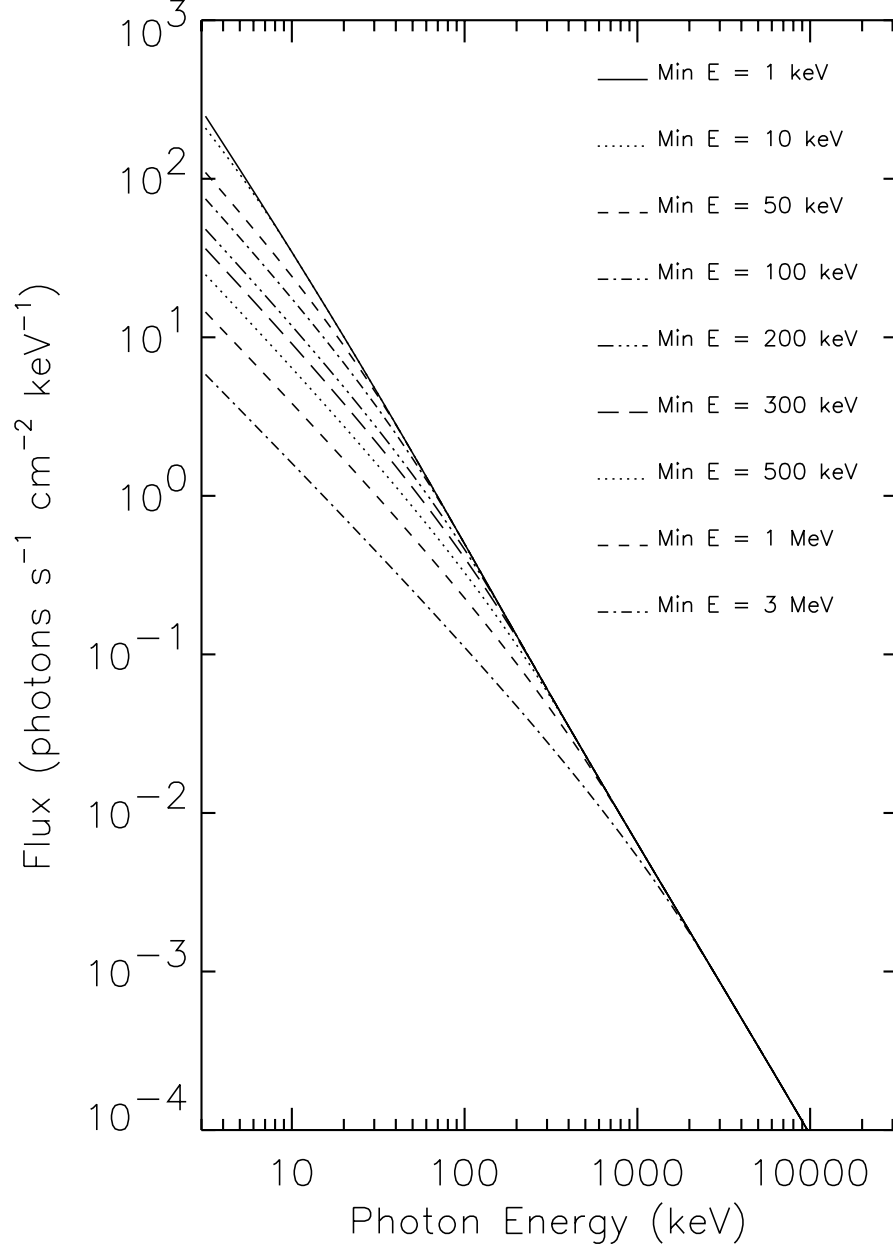


Fig. 7.— Thick-target bremsstrahlung spectra for Case 1 input parameters and low-energy cutoffs in the electron distribution at 1 keV (solid line), 10 keV (upper dotted line), 50 keV (upper short dash), 100 keV (upper dot dash), 200 keV (dash and three dots), 300 keV (long dashes), 500 keV (lower dotted line), 1 MeV (lower short dash), and 3 MeV (lower dot dash). The high-energy cutoff is fixed at 3 GeV.

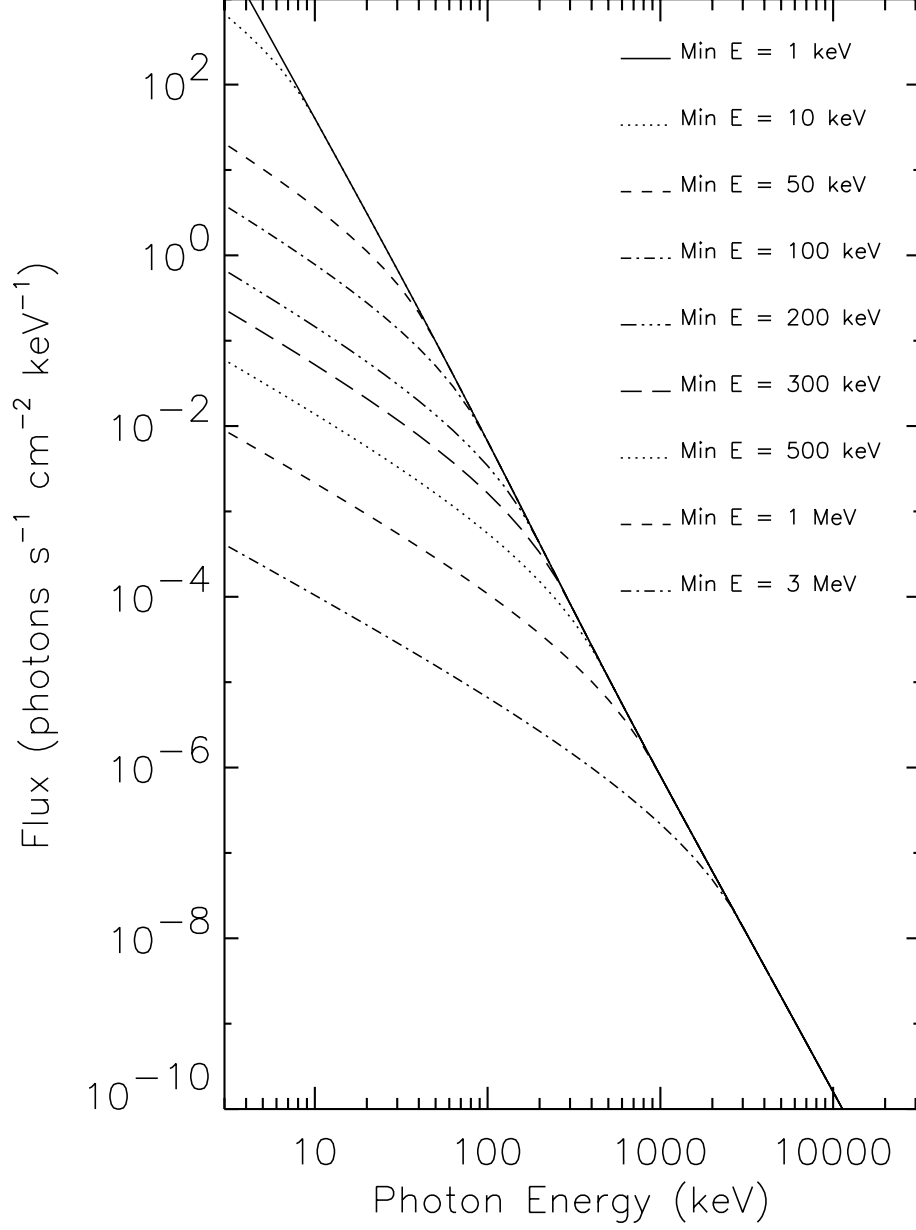


Fig. 8.— Thick-target bremsstrahlung spectra for Case 2 input parameters and low-energy cutoffs in the electron distribution at 1 keV (solid line), 10 keV (upper dotted line), 50 keV (upper short dash), 100 keV (upper dot dash), 200 keV (dash and three dots), 300 keV (long dashes), 500 keV (lower dotted line), 1 MeV (lower short dash), and 3 MeV (lower dot dash). The high-energy cutoff is fixed at 3 GeV.

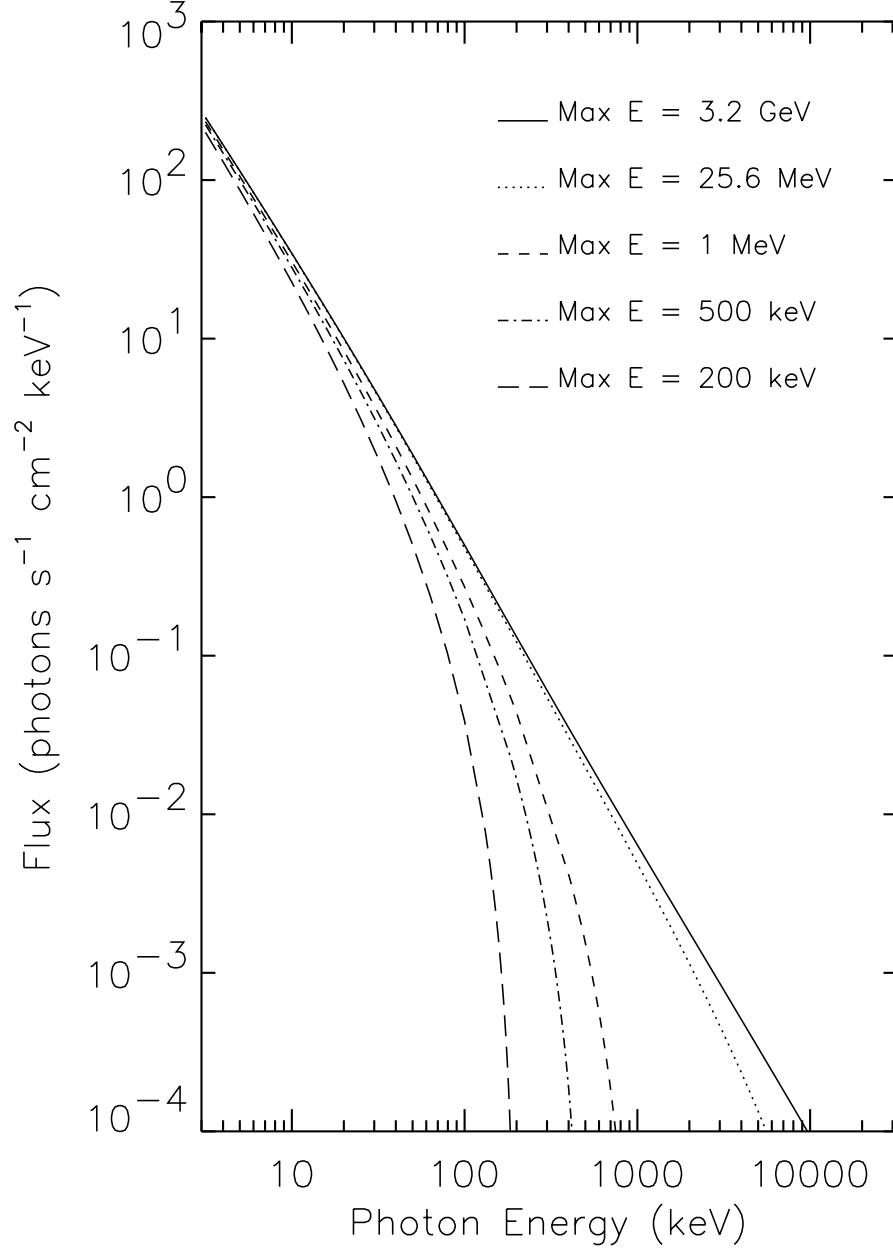


Fig. 9.— Thick-target bremsstrahlung spectra for Case 1 input parameters and high-energy cutoffs in the electron distribution at 3.2 GeV (solid line), 25.6 MeV (dotted line), 1 MeV (short dash), 500 keV (dot dash), and 200 keV (long dash). The low-energy cutoff is fixed at 1 keV.

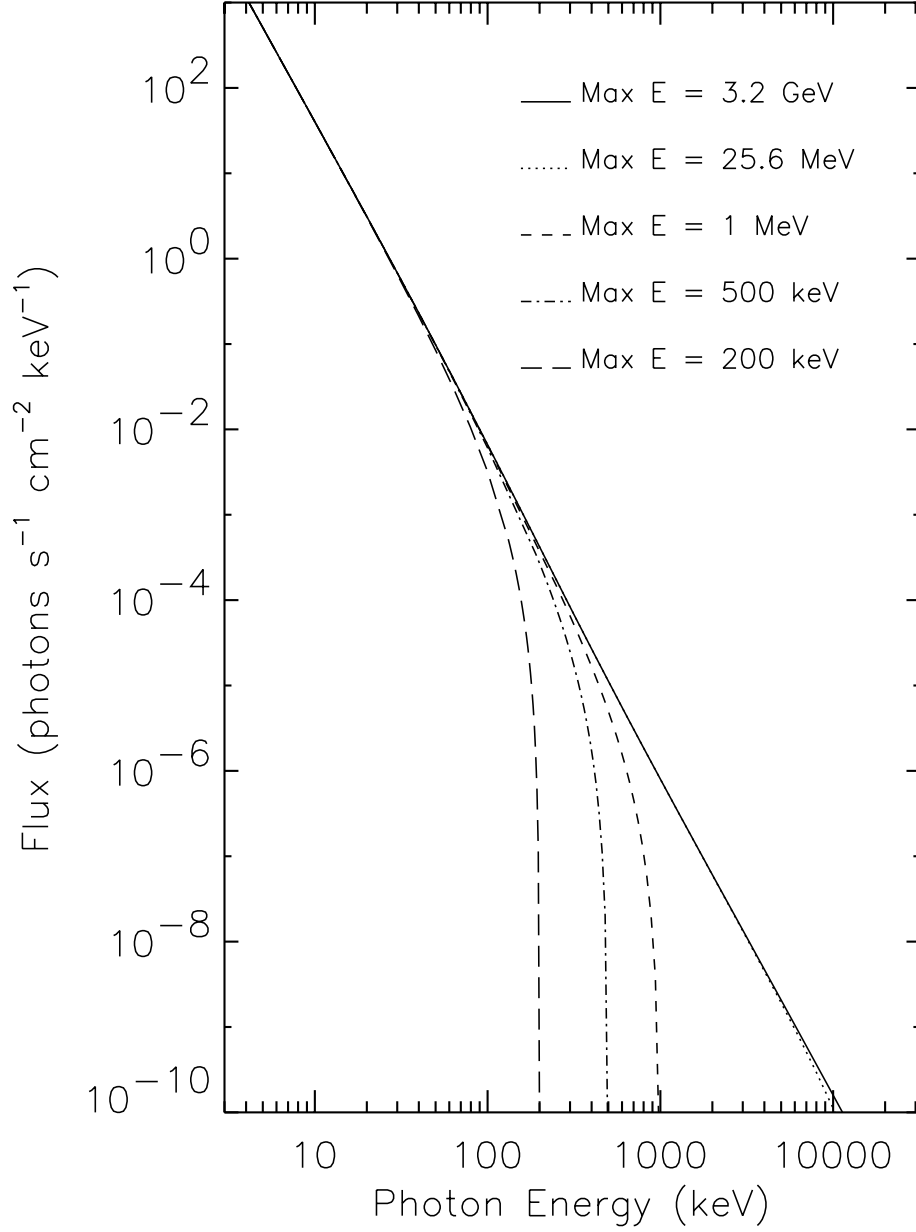


Fig. 10.— Thick-target bremsstrahlung spectra for Case 2 input parameters and high-energy cutoffs in the electron distribution at 3.2 GeV (solid line), 25.6 MeV (dotted line), 1 MeV (short dash), 500 keV (dot dash), and 200 keV (long dash). The low-energy cutoff is fixed at 1 keV.

Table 1. Input Parameters

Case	B (G)	θ	n_{th} (cm ⁻³)	K	δ	L (cm)	A (cm ²)
1	300	45°	6.08×10^9	2×10^9	3	1×10^9	1×10^{18}
2	300	45°	6.08×10^9	4×10^{12}	5	3×10^9	1×10^{18}
3	100	45°	6.08×10^9	2×10^{10}	3	3×10^9	1×10^{18}